NeuroImage 186 (2019) 43–55

Contents lists available at ScienceDirect

NeuroImage

journal homepage: www.elsevier.com/locate/neuroimage

Diffusion tensor imaging shows mechanism-specific differences in injury pattern and progression in rat models of acute spinal cord injury

Andrew Yung [a,*], Stephen Mattucci [b], Barry Bohnet [a], Jie Liu [b], Caron Fournier [b], Wolfram Tetzlaff [b], Piotr Kozlowski [a,b], Thomas Oxland [b]

[a] University of British Columbia MRI Research Centre, 2221, Wesbrook Mall, M10 Purdy Pavilion, Vancouver, BC V6T 2B5, Canada
[b] ICORD, 818 W. 10th Ave., Vancouver, BC V5Z 1M9, Canada

ARTICLE INFO

Keywords:
MRI
DTI
Segmentation
Longitudinal diffusivity
Spinal cord injury

ABSTRACT

We investigate the ability of diffusion tensor imaging (DTI) to distinguish between three experimental rat models of spinal cord injury mechanism – contusion, dislocation, and distraction. Ex vivo DTI scans were performed on cord specimens that were preserved at different time points of the acute injury (3 hr, 24 hr, and 7 days post-injury) across all three injury mechanisms. White matter was classified as abnormal if their DTI metric was substantially different from regional values measured from a set of uninjured controls, thus allowing generation of binary "white matter damage maps" which categorizes each pixel in the DTI image as "normal" or "damaged". Damage classification was most robust using thresholds in the longitudinal diffusivity, which supports previous studies that show that longitudinal diffusivity is the most robust DTI metric in depicting damage in SCI. Furthermore, the spatial damage patterns from all subjects in the same group were consolidated into a "damage occurrence ratio map", which illustrates an average damage shape that characterizes the injury mechanism. Our analysis has yielded a dataset which highlights the differences in injury pattern due to the initial mode of mechanical injury. For example, contusion produced an initial injury that emanated radially outward from the central canal, with subsequent damage along the caudal corticospinal tract and rostral gracile fasciculus; dislocation injuries showed a high level of involvement in the lateral and ventral white matter which became less apparent by 7 days post-injury, and distraction injuries were found to be less focal and more distributed rostrocaudally. This work represents a first step in adopting the use of the primary injury mechanism as a clinical prognostic factor in SCI, which may help to inform the trialing of existing neuroprotective treatment candidates, the development of new therapies as well as personalize the management of SCI for the individual patient.

1. Introduction

The treatment of spinal cord injury (SCI) continues to be a heavily researched topic due to the devastating effects on patients and the high cost to society. Despite decades of research and about a dozen clinical trials, no effective treatment has thus far been found for neuroprotection of the acutely injured spinal cord. This lack of success may be explained in part by the difficulty to predict spontaneous recovery due to the heterogeneity of injury among patients. One possible predictive factor that has been identified is the initial injury mechanism (i.e. the mechanical mode of injury), which has long been recognized as having an influence on neurological dysfunction (Tator, 2006). For example, SCI may manifest with various injury patterns such as fracture dislocations, which leads to poorer functional outcomes than other injury types such as burst fractures (Sekhon and Fehlings, 2017; Pickett et al., 2006). The different internal strain distributions produced by each injury mechanism leads to variations in the initial spatial pattern of damage (Russell et al., 2012; Khuyagbaatar et al., 2016; Bhatnagar et al., 2016), which may further influence the complex cascade of continued damage known as secondary injury. However, despite these known effects on neurological pathology and dysfunction, current clinical treatment trials do not differentiate between injury mechanisms to the spinal cord, thus ignoring potentially important differences.

We have explored this theme of injury mechanisms in SCI through the development of a novel multi-mechanism injury device for experimental rat models of SCI, and through the characterization of the resultant

* Corresponding author. 2221 Wesbrook Mall, M10 Purdy Pavilion, V6T 2B5, Canada.
E-mail addresses: ayung@mail.ubc.ca (A. Yung), mattucci.stephen@gmail.com (S. Mattucci), bbohnet@phas.ubc.ca (B. Bohnet), jliu@icord.org (J. Liu), cfnbub@gmail.com (C. Fournier), tetzlaff@icord.org (W. Tetzlaff), piotr.kozlowski@ubc.ca (P. Kozlowski), toxland@icord.org (T. Oxland).

https://doi.org/10.1016/j.neuroimage.2018.10.067
Received 9 February 2018; Received in revised form 19 October 2018; Accepted 25 October 2018
Available online 26 October 2018
1053-8119/© 2018 Elsevier Inc. All rights reserved.

Abbreviations:

3hr	3 hours
24hr	24 hours
7d	7 days
CST	Corticospinal tract
DTI	diffusion tensor imaging
D_{long}	longitudinal diffusivity
Injured D_{long} area fraction	fractional area in D_{long} parameter map that is classified as below normal
D_{trans}	transverse diffusivity
FA	fractional anisotropy
GM	gray matter
MAD	median absolute deviation
PF	paraformaldehyde
SCI	spinal cord injury
SNR	signal to noise ratio
TrW	trace-weighted signal intensity
WM	white matter

pathology and behavioural deficits (Choo et al., 2007, 2008, 2009; Chen et al., 2015). This device is able to reproducibly inflict contusion and dislocation SCI mechanisms, which aim to simulate the two most common forms of human injury patterns seen in the clinic (burst fractures and fracture-dislocations, respectively). Distraction SCI mechanisms have also been explored using the same rig, which may help to understand a less common injury pattern known as flexion-distraction, whereby a flexion moment tends to apply posterior distractive forces that axially stretch the spinal cord. Thus far, we have found intriguing differences in the pathology and behavioural deficits between injury mechanisms.

Any potential prognostic factor for SCI outcomes requires an appropriate biomarker to detect these differences clinically. A readout that is sensitive to white matter damage would be particularly interesting, since it is certainly a hallmark of both the initial mechanical insult and progressive secondary injury. Diffusion tensor imaging (DTI) shows particular promise in filling this role, arguably providing more information than the conventional T1-and T2-weighted MRI that is typically used for spinal cord imaging. DTI is already widely available on clinical MRI scanners, largely for imaging of the brain. A number of studies in both rodent models (Budde et al., 2007; Kim et al., 2007, 2009, 2012; Loy et al., 2007; Ellingson et al., 2008, 2010; Deo et al., 2006) and humans (Cheran et al., 2011; Sasiadek et al., 2012; Koskinen et al., 2013; Hendrix et al., 2015; Shanmuganathan et al., 2017) have posited that the resultant parametric maps derived from the diffusion imaging experiment are related to different aspects of white matter damage in the spinal cord: fractional anisotropy (FA) and longitudinal diffusivity (D_{long}) has been shown to be sensitive to axonal damage, while transverse diffusivity (D_{trans}) changes may be related to damage across the myelin sheath (Kim et al., 2007; Loy et al., 2007; Tu et al., 2013). The use of diffusion weighted MRI in spinal cord injury is an active area of research, with efforts to improve the specificity of the parametric maps through modeling (Cohen-Adad et al., 2008, 2017; Nossin-Manor et al., 2007; Xu et al., 2014), as well as to address the numerous technical challenges to translating these methods to the clinic (Stroman et al., 2014; Figley and Stroman, 2007; Smith et al., 2012; By et al., 2016).

The goal of this work was to investigate the ability of DTI to characterize the differences in injury due to the initial mechanism, using our experimental rat models of contusion, dislocation and distraction. Ex vivo DTI scans were performed on cord specimens that were preserved at different time points of the acute injury (3 h, 24 h, and 7 days post-injury) across all three SCI mechanisms of contusion, dislocation, and distraction. We hypothesize that DTI is able to distinguish mechanism-specific differences in the spatial pattern of injury and its temporal progression in acute SCI. To this end, we take the approach of Kim et al.,2009 to segment areas of white matter damage by comparing the DTI metrics in an injured cord to reference values generated from a set of uninjured controls. This allows the generation of a "white matter damage map" which classifies each pixel in the DTI image as "normal" or "damaged". Furthermore, the spatial damage patterns from all subjects in the same group are consolidated into a "damage occurrence ratio map", which illustrates an average damage shape that characterizes the injury mechanism at a certain acute time point after initial injury. In this way, we aim to provide evidence that DTI can be a useful technique to show differences in the temporal and spatial evolution of injury that is caused by the mode of initial mechanical insult. Conceivably, knowledge of the mechanism of primary injury (as determined by conventional MRI or CT) could be used by clinicians to predict which tracts are most affected by the injury as well as the timeline of injury progression, with DTI providing a method to verify the prognosis over time.

2. Methods

2.1. Injury models

Figure 1 schematically describes the three different injury models used in this study: contusion (dorsal compressive impact from an actuator tip), dislocation (dorsoventral shearing of the spinal cord), and distraction (stretching of cord along the rostrocaudal axis). All procedures were approved by our institution's Animal Care Committee in accordance with the guidelines published by the Canadian Council on Animal Care. Ninety-four male Sprague-Dawley rats were included in the data analysis (see Table 1 for allocation of experimental groups, as well as a tabulation of rejected subjects with explanations) at an average weight of 311 ± 14 g at the time of surgery. Moderate contusion, dislocation, and distraction were produced at C5/C6 levels, using the UBC multi-mechanism SCI apparatus (Choo et al., 2007, 2008, 2009; Chen et al., 2015). The injury and post-injury procedures are detailed in Chen et al. (2015), but with the following differences: a 15° flexion was applied in the distraction injury (as outlined in Choo et al., 2009), slightly different actuator displacements (1.30 ± 0.01 mm for contusion, 1.77 ± 0.07 mm for dislocation, and 4.37 ± 0.14 mm) and an additional dose of buprenorphine per day in the initial recovery period (three daily doses).

Five sham animals were also included in the MRI scanning and analysis. Two of these animals served as controls for the contusion injuries, with the laminectomy performed as well as preload application of the actuator tip on the dura mater. The remaining three shams served as controls for the distraction injuries, subject to the same clamp fixation for injury, but only a 2 N rostral preload applied.

2.2. Tissue processing and histology

Animals were sacrificed at predetermined time points at 3 hours (3hr) 24 hours (24hr) and 7 days (7d) post-injury by an overdose of 5% chloral hydrate (intraperitoneal injection), and perfused with 0.9% phosphate buffered saline, followed by phosphate-buffered 4% paraformaldehyde (PF). Spinal cords were harvested and post-fixed in PF for 24 h; MRI scans were performed during this fixation period between 19 and 25 hours after harvesting. Spinal cords were then submerged in progressive sucrose solutions (12%, 18%, 24%) every 24 h, then frozen in embedding (OCT) compound. A number of representative cords were sectioned in the transverse plane at 20 μm thickness, and divided into 10 interleaved sets. One of these sets, with sections spaced 200 μm apart, was immunostained for myelin and axon content. Sections were blocked for 30 minutes in normal donkey serum (1:10, Jackson ImmunoResearch Laboratories, West Grove, PA) before incubation overnight at room temperature in primary antibodies diluted in 0.01 M PBS with 0.1% Triton X-100. Primary antibodies were used to target myelin basic protein (MBP) (chicken host, 1:200, Aves Labs, Tigard, OR), Neurofilament-H (NF-H) (mouse host, 1:500, Abcam, Toronto, ON), β-tubulin III (Tub)

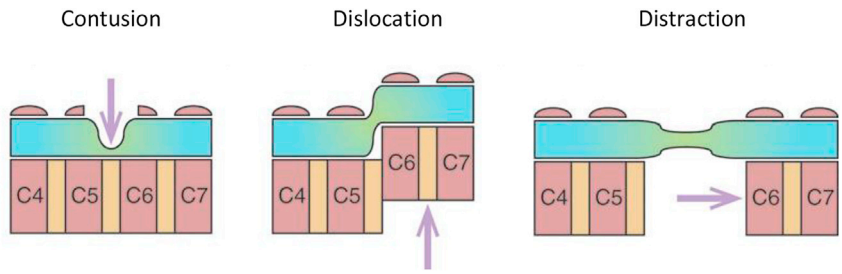

Fig. 1. Schematic illustrating the different injury mechanisms. Contusion (focal compression), dislocation (shearing), and distraction (tensile stretch) are shown.

Table 1
Experimental group numbers.

Experimental group	# included	# rejected (acquisition issues)	# rejected (injury mechanism issues)
Contusion			
3 hr	10	–	2[f]
24 hr	9	–	1[c]
7 d	9	1[a],1[b]	–
Dislocation			
3 hr	9	1[a]	1[d], 5[h]
24 hr	10	4[b], 1[a]	2[d], 2[f]
7 d	12	–	4[g]
Distraction			
3 hr	11	–	1[f]
24 hr	9	1[a]	1[e]
7 d	10	1[a]	1[h]
Sham			
	5	–	–
Total	94	10	20

[a] Ghost artifacts on diffusion-weighted images.
[b] Coil malfunction – low signal to noise ratio (SNR).
[c] Only left side of cord was injured, as observed on MRI.
[d] Procedural error.
[e] No pre-flexion was applied in distraction injury.
[f] Perished immediately or within 24 h post-injury.
[g] Humane endpoint reached (i.e. demonstrated severe weight loss, respiratory issues, porphyrin, etc.).
[h] Broken lamina or vertebral clamp slipped.

(mouse host, 1:500, Abcam), and SMI-312 (SMI) (mouse host, 1:500, Covance, Princeton, NJ). Sections were then washed 3 × 5 min in 0.01 M PBS and incubated for 2 h in secondary antibodies conjugated with DyLight 488 (donkey host, chicken antigen, Jackson ImmunoResearch Laboratories, West Grove, PA) and DyLight 594 (donkey host, mouse antigen, Jackson ImmunoResearch Laboratories). Sections were washed 3 × 5 min in 0.01 M PBS then mounted with Fluoromount-G (SouthernBiotech, Birmingham, AL). Sections were processed at the same time under the same conditions to minimize differences due to procedural variability. Sections were imaged under a fluorescence microscope (Axio Observer Z1 inverted confocal) for 5 rostrocaudal locations (±3 mm, ±1 mm, 0 mm relative to epicentre) at six square regions of interest (57.25 μm × 57.25 μm pixel size at 63x magnification) at the following standardized locations: gracile fasciculus (placed 50 μm from midline, small axons), cuneate fasciculus (placed 50 μm from gray matter dorsal horn and corticospinal tract), dorsal corticospinal tract (placed 50 μm from gray matter, very small axons), dorsolateral WM (placed 50 μm from gray matter dorsal horn), and lateral WM (placed lateral to the gray matter, at the dorsoventral midline). In regions where different parts of the tissue came into focus at different Z-stack levels (due to the tissue section not being flat), the individual Z-stack images were collapsed into one image by an extended depth of field algorithm (Aguet et al., 2008) implemented in ImageJ/Fiji (Schindelin et al., 2012). A survey image at 10x magnification was acquired which was used to annotate the locations of the 63x magnification images.

2.3. Ex vivo DTI acquisition and data processing

The cord specimens were loaded into 1 mL syringes filled with 4% paraformaldehyde in PBS and stabilized by a parallel plastic rod. MR images of these specimens were acquired with a 7 Tesla Bruker Biospec 70/30 USR preclinical scanner with 400 mT/m gradients, using a 59 mm quadrature volume coil for transmit and a stripline coil for receive (Jasiński et al., 2012). RARE T2-weighted scans were acquired to locate the epicentre of the injury (manually identified as either a punctate hypointensity or as the midpoint of disrupted gray and white matter anatomy). After magnetic field shimming based on an acquired field map, eleven 1 mm thick slices arranged around the epicentre were acquired for diffusion tensor imaging (sequence parameters: spin echo DTI-EPI, 8 shots, b = 1000 s/mm^2, δ = 3.5 ms, Δ = 12 ms, 6 icosahedral directions and one b = 0 image, 18 averages, TE/TR = 38.61/2750 ms, matrix = 128 x 128, FOV = 6.4 × 6.4 mm, 50 μm in-plane resolution, acquisition time = 46 min 12 s).

The pixel-wise diffusion tensor data were diagonalized to calculate the principal diffusivities (λ_1, λ_2, λ_3), which were used to derive the fractional anisotropy (FA), longitudinal diffusivity (D_{long}), and transverse diffusivity (D_{trans}) according to the following equations:

$$FA = \sqrt{\frac{3}{2}\frac{(\lambda_1 - MD)^2 + (\lambda_2 - MD)^2 + (\lambda_3 - MD)^2}{\lambda_1^2 + \lambda_2^2 + \lambda_3^2}} \quad MD = \frac{\lambda_1 + \lambda_2 + \lambda_3}{3} \quad D_{long} = \lambda_1 \quad D_{trans} = \frac{1}{2}(\lambda_2 + \lambda_3) \qquad [1]$$

The trace-weighted (TrW) image was generated for use in image segmentation and examination of hemorrhage patterns according to equation [2] (A_o is the signal intensity of the image set acquired without diffusion weighting, b is arbitrarily set to 1000 s/mm^2), due to adequate contrast between white matter, gray matter and paraformaldehyde fluid within the lesion cavity.

$$TrW = A_o e^{-b\frac{\lambda_1+\lambda_2+\lambda_3}{3}} \qquad [2]$$

Each cord was manually segmented in 3D Slicer (NA-MIC, www.slicer.org) to mask out the exterior perfusate, delineate the white matter/gray matter boundary, and divide the white matter into transverse sectors (dorsal, ventral, and lateral), using the TrW image as well as T2-weighted images that were also acquired (RARE, TE_{eff}/TR = 46/1500 ms, RARE factor = 4, number of averages = 6, matrix = 192 x 192, FOV = 9.6 × 9.6 mm, 1 mm slice thickness). Where GM/WM image contrast near the injury epicenter became too low, delineation was subjectively guided by trying to maintain the spatial smoothness of the gray matter volumetric shape. Hemorrhage area throughout individual slices were manually segmented as hypointense regions in the TrW images.

2.4. Generation of white matter damage map

The general spatial distribution of white matter damage is made more tractable by generating a "white matter damage map", which is a binary mask that classifies each white matter pixel as either "damaged" or

"normal", based on how close its DTI metric is to the regional average derived from a set of uninjured cords. The specific details of generating this map are shown in Fig. 2, using D_{long}, or FA or D_{trans} as the metric of interest. For each rostrocaudal position and transverse area of the white matter (dorsal, ventral, and lateral), the D_{long} (or FA) pixel values from all control cords are assembled into a histogram, from which the median and median absolute deviation of the uninjured distribution is calculated. The median absolute deviation (MAD) is calculated by taking the residuals around the median, and then taking the median of their absolute values (analogous to standard deviation, but around the median). The median minus one MAD is considered the region's cutoff value for classifying pixels in the injured cords: if the D_{long} (or FA) in a corresponding slice and transverse ROI is lower than this cutoff value, then the pixel is classified as damaged. Fig. 2d schematically shows the damage map as being red within "injured" areas and green within "normal" areas, as predicted by D_{long} or FA.

Generation of a white matter damage map from D_{trans} proceeds in a similar fashion, except that damage is predicted by D_{trans} values that are above the median plus one MAD deviation of the control group data, since an elevated D_{trans} has been associated with white matter damage (Tu et al., 2013).

2.5. Generation of damage occurrence ratio map

In order to visualize the spatial patterns of damage from the large amount of data acquired, the white matter damage maps from each experimental group were consolidated into a "damage occurrence ratio map" (see Fig. 3), which represents the typical damage pattern for each injury/time point group. For each slice position, gray matter and white matter (GM/WM) masks were manually defined for all cords. The GM/WM mask of one cord from each group was chosen as a reference geometry, to which all other cords in the same group were registered on a slice-by-slice basis. This image registration was performed by the detection of 200–300 points along the exterior and gray matter perimeter for each rostrocaudal slice (using the Canny edge detection algorithm (Canny, 1986) and registered automatically using the Coherent Drift Point (Myronenko and Song, 2010) algorithm. The deformation fields that result from the GM/WM image registration are used to warp the corresponding white matter damage maps, so that all pixels in the warped damage maps are putatively in the same reference frame. The Damage Occurrence Ratio map is calculated simply as the number of times a pixel at that location was classified as damaged, divided by the total number of cords. The value of this metric ranges from zero (none of the cords showed damage) to one (all cords showed damage at this location). The result is a heatmap of how often a particular location was classified as damaged.

2.6. Statistical analysis

For each transverse sector and rostrocaudal location, injured group ROI averages of D_{long}, FA, and D_{trans} were compared to the corresponding control values using a Student's t-test if the distribution was normal, and a Mann-Whitney test when normality could not be assumed. A p-value threshold of 0.05 was used to detect a statistically significant difference.

As a numeric representation of the damage pattern, the area fraction occupied by D_{long}-classified damaged pixels (injured D_{long} area fraction) was calculated for each transverse sector at each rostrocaudal position. SPSS (IBM, USA, version 24.0) was used to perform statistical analysis.

For each group of these data samples (specific mechanism, timepoint, transverse sector and rostrocaudal position), significant outliers were detected if the magnitude of the studentized residuals was greater than 3 standard deviations (Cook and Weisberg, 1982), and a normal distribution was assumed if the Shapiro-Wilk test produced a p-value greater than 0.05. Amongst all injured D_{long} area fraction distributions (total of 3 mechanisms x 3 timepoints x 11 rostrocaudal locations x 3 transverse sectors = 297 datasets), 98% of the groups had no significant outliers and 97% of groups met the assumption of normality.

Two-way mixed ANOVA was applied for each injury mechanism and transverse sector pairing, to test for main effects of time post-injury (the between-subjects factor, since time points were studied with separate groups), the rostrocaudal location (the within-subjects factor), and statistically significant interactions between the two factors. If such an interaction was found, differences between post-injury time at specific rostrocaudal locations were assessed using Tukey's test at a threshold level of $p = 0.05$. If no significant interaction was found, we tested if the main effect of time post-injury across all rostrocaudal locations was statistically significant, which was followed up by pairwise comparisons (with Bonferroni adjustment for multiple comparisons) to detect where the differences occur at a threshold level of $p = 0.05$.

3. Results

3.1. Choice of D_{long} cutoff value for generation of WM damage map

The D_{long} cutoff value used for generation of the WM damage map was chosen to be median – 1*MAD as measured in a set of uninjured shams. The white matter damage map for a typical sham cord that was generated with the current cutoff value is shown in Fig. 4a. Some isolated pixels were misclassified due to noise, but there was also evidence of systematic misclassification in the inner lateral white matter as well as

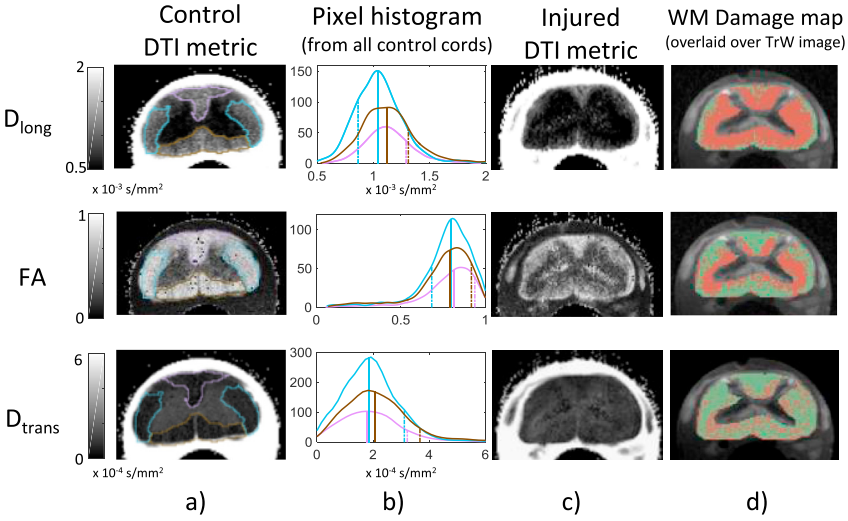

Fig. 2. Generation of white matter damage map using D_{long}, FA or D_{trans}. (a) For each slice in all control cords, white matter pixels are segmented into dorsal, lateral and ventral sectors. (b) For a particular slice and white matter sector, the cutoff value (dashed line) between "normal" and "damaged" is determined from all control cord pixels in that region as the median value minus one median absolute deviation (for D_{long} and FA) or median plus one median absolute deviation (for D_{trans}). (c) Each pixel in the injured map is compared to its region's cutoff value. (d) Parameters values below its slice/sector cutoff value are considered to be damaged (marked in red, overlaid on the trace-weighted image). Injured cord shown was from the dislocation 7 day post-injury group.

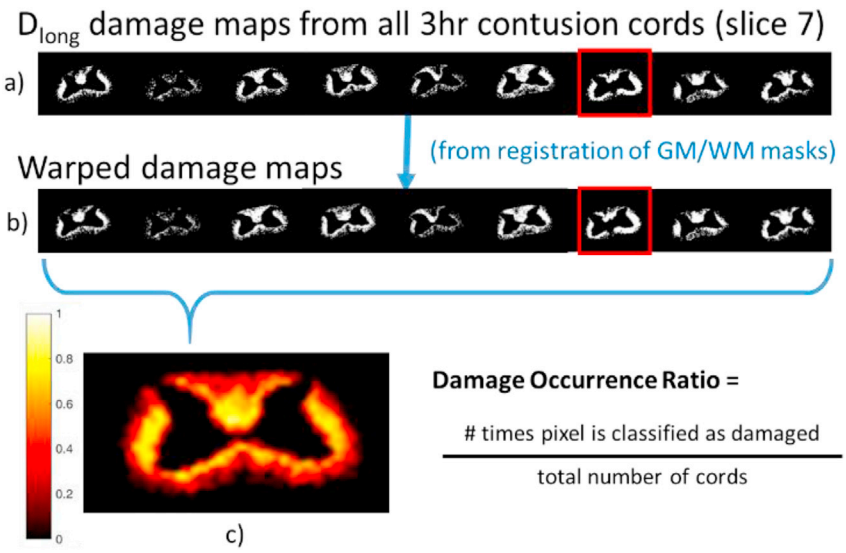

Fig. 3. Calculation of the Damage Occurrence Ratio. This represents the average damage pattern for one injury/time point group (shown here for D_{long}-predicted damage at 1 mm caudal for the 3-hour contusion group). For each slice position, GM/WM masks from all cords in the same group are registered to one manually chosen subject (highlighted with red box), resulting in the damage maps being warped from their original shape (a) to a standard reference cord shape (b). The damage occurrence ratio is c) the number of times a pixel is classified as damaged, divided by the total number of cords.

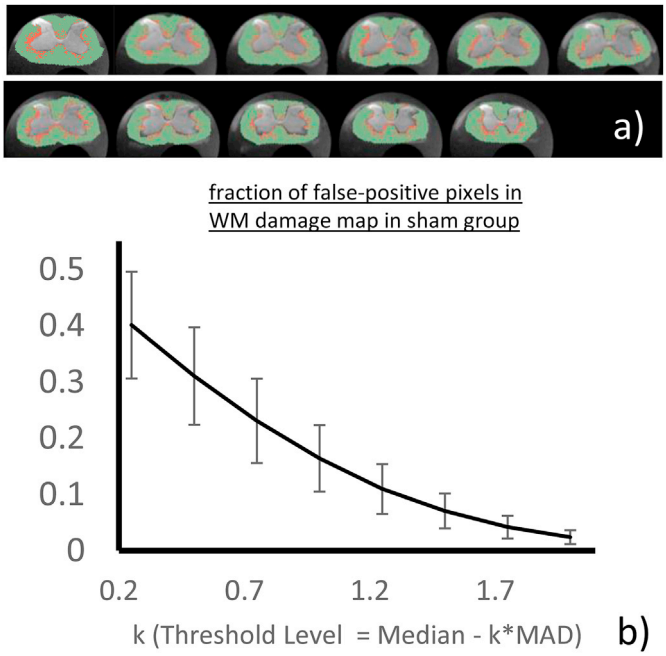

Fig. 4. Misclassification of damage in uninjured sham cords. a) White matter damage map of a typical uninjured sham cord, with red depicting areas where D_{long} was below chosen threshold value. b) Whole-cord fraction of misclassified pixels in WM damage map as a function of threshold value (median – k*MAD). k = 1 corresponds to current choice.

the corticospinal tract, which suggests that the uninjured DTI values in these regions may be appreciably different than the rest of the ROI (dorsal WM and lateral WM, respectively). This may perhaps be due to regional differences in axon size and distribution (for example, a recent paper (Zaimi et al., 2018) which derived several axonal geometry parameters from EM histology shows that CST in rat has much smaller and densely packed axons than the rest of the dorsal WM, whereas the inner lateral white matter has slightly smaller and more densely packed axons than the outer lateral white matter).

To quantify the effect of the cutoff value on specificity, white matter damage maps of the sham cords were generated at a variety of threshold values (cutoff value = median – k*MAD, with k ranging from 0.2 to 2), and the mean fraction of false-positive pixels per cord was plotted as shown in Fig. 4b. As expected, cutoff values closer to the uninjured median values resulted in a higher number of false positives. The current choice of cutoff value (k = 1) resulted in 16 ± 6% of the white matter pixels being misclassified as damaged in the uninjured shams. A threshold of median – 0.5*MAD leads to an average false positive rate of 31±10%, whereas a cutoff of median – 1.5*MAD leads to 7±3% misclassification.

3.2. DTI metric group averages

For a particular rostrocaudal position and transverse sector, the ROI mean values of D_{long}, D_{trans}, and FA were calculated from each subject and used to form group averages for each injury/time point group (see Fig. 5). Rostrocaudal position and the transverse sector location are denoted by x-axis position and data series colour, respectively. Error bars represent standard error of the mean. The ROI averages for the control group are shown as dashed lines to illustrate how far the injured ROI averages are from an uninjured value. A statistically significant difference between an injured mean and control mean is denoted by a solid filled circle on the injured data series.

D_{trans} was judged to be the least effective parameter for detecting abnormalities in white matter, since it showed the least number of significant differences between injured and control. This observation is borne out by the white matter damage maps generated from D_{trans}, which show only a small diffuse fraction of pixels that can be classified as abnormal (see Fig. 2). However, the evolution of D_{trans} for the contusion model shows a clear trend of increasing injury over time, which suggest that changes in D_{trans} may continue to develop at later time points. D_{long} and FA show better dynamic range, with similar levels of separation between injured and uninjured values near the epicentre. However, D_{long} shows clearer significant differences at the rostrocaudal extents, showing that damage predicted by D_{long} extends throughout the entire 11 mm length of cord that was studied (equivalent to approximately four vertebral levels). In comparison to D_{long}-derived white matter damage maps, the spatial patterns of damage predicted by FA followed the same shapes, but were in general smaller and more focused around the gray matter, as briefly illustrated in Fig. 2d. Data analysis and presentation of results therefore concentrate on using D_{long} as the metric that was most useful in observing differences between injury models and time points (damage occurrence ratio maps for FA are shown in the Appendix).

3.3. Characterization of spatial and temporal injury patterns

In an analogous fashion to Fig. 5 and Fig. 6 represents the average

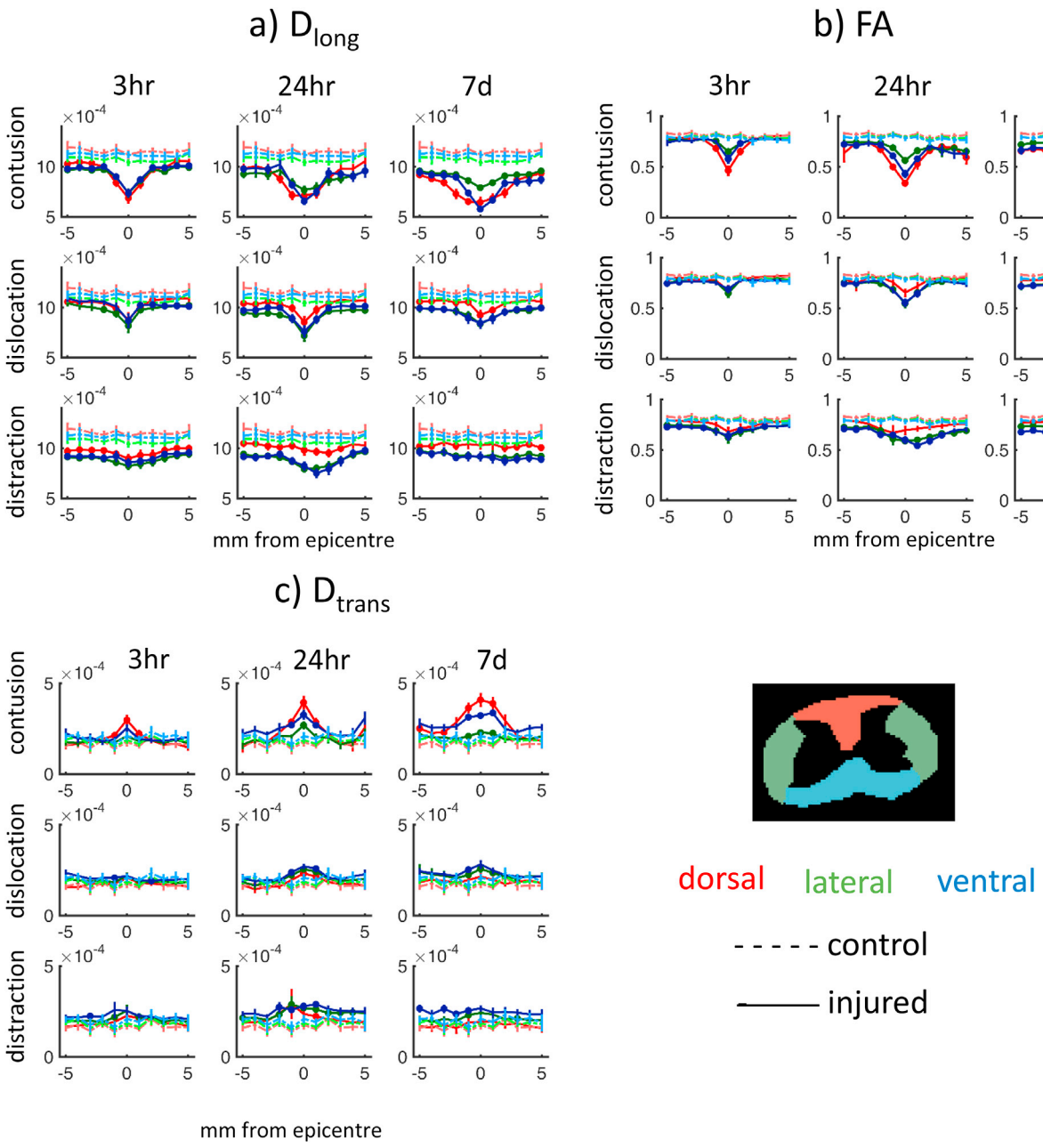

Fig. 5. Transverse group averages of DTI parameters. ROI averages of a) D_{long}, b) FA and c) D_{trans}, shown along rostrocaudal position relative to injury epicentre (negative positions are rostral). Error bars represent standard error of the mean. Injured and corresponding uninjured control mean values are shown by solid and dashed lines, respectively. A statistically significant difference ($p < 0.05$ using Student's t-test or Mann-Whitney test) between an injured mean and control mean is denoted by a solid filled circle on the injured data series.

fractional area of D_{long} pixels that are classified as "damaged" for a particular rostrocaudal position and transverse sector (denoted as injured D_{long} area fraction). Fig. 7 shows the damage occurrence ratio maps as predicted by D_{long}, which visually communicates the average shape of white matter damage (recall that ratio values close to one, denoted in yellow, represent areas where most cords in each experimental group showed damage). Taken together, Figs. 6 and 7 were examined to draw qualitative conclusions about how the shape and evolution of injury differ across injury mechanisms, supported by statistical analysis to study differences between post-injury time points. Table 2 summarizes the statistical results (p value and F-statistic) where there was a statistically significant difference across time post-injury for a particular mechanism and transverse/rostrocaudal location.

3.3.1. *Contusion*

The damage occurrence ratio maps for the contusion group show a focal, roughly spherical central injury at 3 h post-injury, with progressive spread of dorsal damage concentrating in the corticospinal tract (CST) and gracile fasciculus in the caudal and rostral directions, respectively. In a qualitative sense, the contusion model exhibits a general monotonic increase in damage area over time, in comparison to the other injury models. The difference in dorsal damage area between 3 h and 7 day groups reached statistical significance throughout most of the spinal cord except for the three central slices; differences between 3 h and 24 h were less robust with only 2 mm rostral showing significant differences. The lateral white matter damage area increases between 3 h and 24 h caudal to the epicentre (statistically significant between 2 and 4 mm caudal).

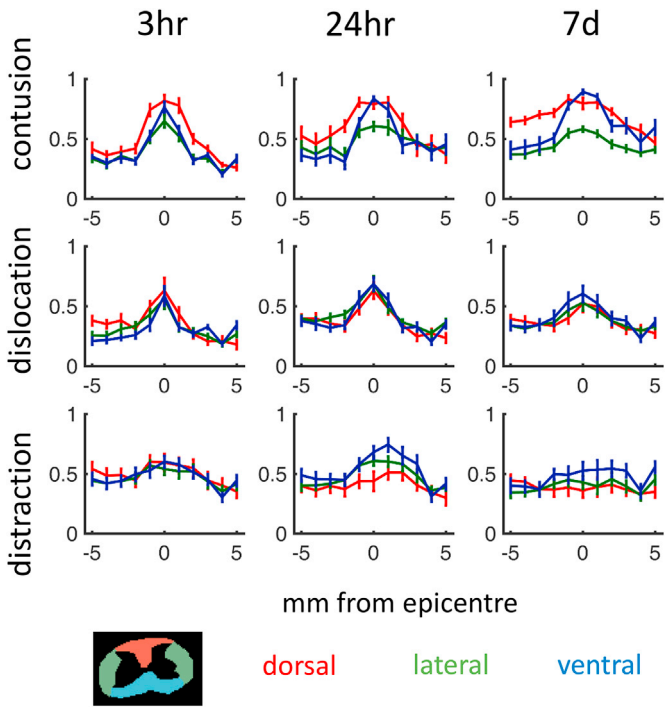

Fig. 6. Transverse group averages of injured D_{long} area fraction. This metric is the fractional area occupied by pixels with D_{long} classified as abnormal, shown for rostral to caudal positions relative injury. Error bars represent standard error of the mean.

Only the 4 mm caudal position showed any difference between 3 h and 7 days in the lateral white matter.

3.3.2. Dislocation

Initial damage in the dislocation model concentrated around the CST, lateral and ventrolateral white matter. The damage occurrence ratio maps suggest that the gracile fasciculus shows less relative damage than other areas of dorsal white matter. Statistical analyses show no significant differences in damage area in the dorsal and ventral white matter between the different time points. However, there was a statistically significant increase in damage area for the lateral white matter across the whole rostrocaudal extent between 3 h and 24 h ($p = 0.048$, $F(2,24) = 3.227$), but this difference is lost by 7 days. The results therefore suggest a peak in lateral damage area at 24 h, which reduces towards the 3 h levels by 7 days.

3.3.3. Distraction

Distraction injury was markedly less focal and more distributed along the rostrocaudal extent. The distraction injury heatmaps in Fig. 7 show most damage in the lateral and ventrolateral white matter, similar to dislocation. Dorsal damage favours the CST, though less so than contusion. No statistically significant differences between post-injury timepoints could be found in the dorsal or ventral damage areas. The only significant difference between time points was found in the lateral white matter, where the damage area decreases from 24 h to 7 days at epicentre and 1 mm caudal. The ventral white matter also shows a trend of damage area peaking at 24 h and a decrease at 7 days post-injury, although no statistically significant difference was found.

3.4. Representative histology images

Figs. 8–10 shows immunostained histology images of representative cords from the 3 h post-injury groups (contusion, dislocation, and distraction respectively), showing the axon and myelin content at a magnification of 63x, along with the corresponding white matter damage maps predicted by D_{long}. These micrographs provide some illustrative examples that qualitatively show what features of the white matter microstructure may underlie the changes in D_{long} at a particular time after injury.

For the 3-hour contusion example (Fig. 8), the micrographs at ±3 mm look qualitatively similar to the sham histology, which corroborates the normative classification in the damage map. The damage map predicts a lack of significant injury in the fasciculus gracilis except for the injury epicentre; accordingly, the histology in these regions look normal except for the epicentre where wholesale loss of white matter is evident. The damage map also seems sensitive to the histologically proven tissue loss and swollen axons within ±1 mm of epicentre in the corticospinal tract and fasciculus cuneatus. In general, the histology corroborates the predictions of the white matter damage map, with perhaps the exception of the dorsolateral and lateral region away from epicentre, where the micrographs still looks qualitatively normal at this early three hour timepoint.

The obvious tissue loss seen in the 3-hour contusion micrographs is much less apparent in the dislocation and distraction examples (Figs. 9 and 10), which may arise from a smaller magnitude of input energy during initial injury, or may show that these injury mechanisms produce different structural hallmarks of neuronal damage. In particular, the distraction injury micrographs (Fig. 10) show no evidence of large cavitation in the tissue, even at epicentre. The distraction example also shows a reduced number of myelinated axons in the dorsolateral white matter as compared to contusion and dislocation, where a dense packing of axons without myelin persists, indicative of an immediate loss in myelin. Both dislocation and distraction micrograph examples show more densely packed axonal tissue, with myelin (MBP-immunoreactive material) without axons, and less circularity, most likely representing myelin debris (see for example the lateral and dorsolateral dislocation micrographs in Fig. 9, at locations rostral to epicentre).

3.5. Hemorrhage pattern

As an ancillary observation, representative examples of hemorrhage patterns as observed in the trace-weighted images are depicted for each mechanism/time point group in Fig. 11a. Only the slices at −1, 0 and +1 mm relative to epicentre are shown. Differences between injury mechanisms can be seen as early as 3 h post-injury: contusion produces a focal hemorrhage with smaller punctate lesions surrounding it, commonly affecting the corticospinal tract (CST) and the central gray matter. Dislocation produces extensive punctate hemorrhage throughout the entire gray matter, while distraction produces a lower number of punctate lesions confined mostly to gray matter. 24 h post injury shows some expansion of the hemorrhage (either in size or an increase in hypointensity), with the 7 day post injury hemorrhage consolidating into a solid crescent-shaped pattern.

The hemorrhage areas for each rostrocaudal position were manually segmented and were summarized for each mechanism/timepoint group as a boxplot, as depicted in Fig. 11b. Hemorrhage areas were generally smaller at 7 days post injury as compared to the 3 h and 24 h time points, with distraction injuries producing smaller hemorrhage areas but wider rostrocaudal extent as compared to the dislocation and contusion injuries. In comparison to the D_{long}-predicted area of white matter damage as shown in Fig. 11c, the hemorrhage areas were generally confined to within 2 mm of epicentre, whereas D_{long} showed damage throughout the 10 mm of cord that was studied. Hemorrhage area also showed more variability than the DTI white matter damage area, as evidenced by the larger number of outliers in the hemorrhage area boxplots.

4. Discussion

The results presented here support the hypothesis that DTI can distinguish between different injury mechanisms in SCI, by examining how the shape and extent of white matter damage evolve over the acute

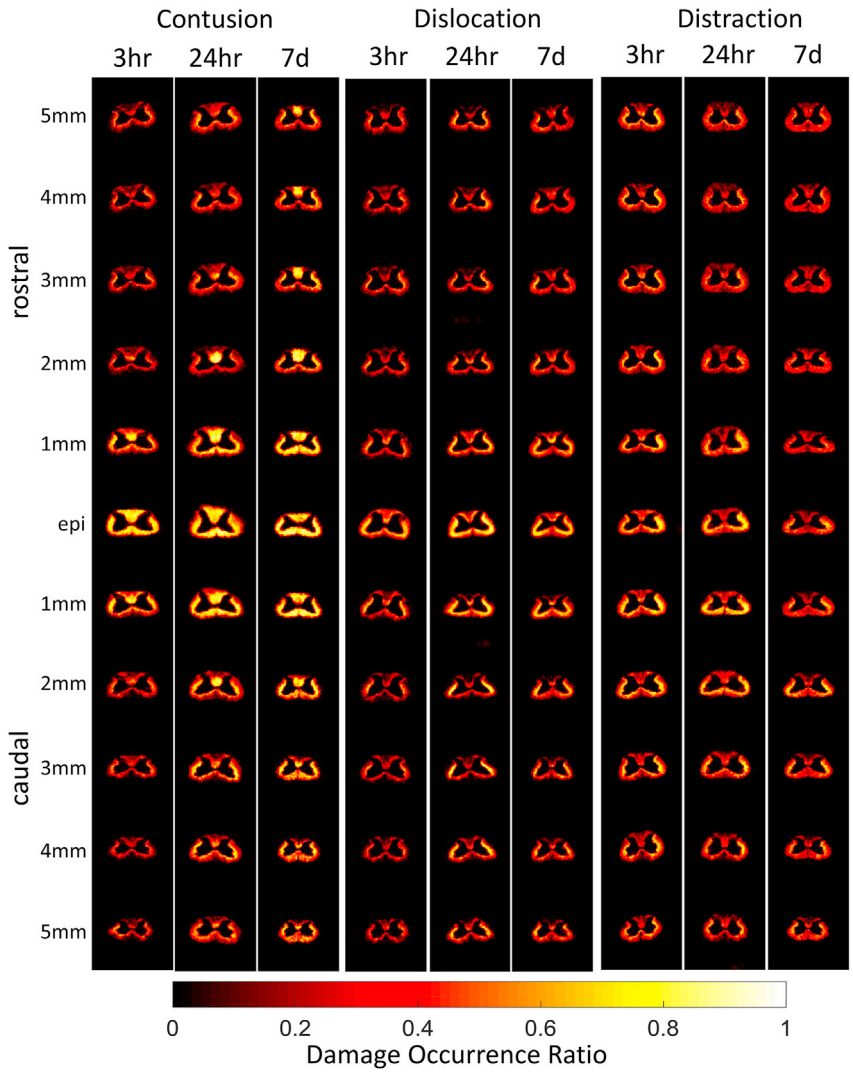

Fig. 7. Damage Occurrence Ratio maps for each experimental group. These spatial maps depict the average damage shape that characterizes each combination of injury mechanism and time post-injury. Transverse slices are shown top to bottom from rostral to caudal.

Table 2
Statistically significant differences in injured D_{long} area fraction across time post-injury.

Injury Mechanism	Transverse sector	Time post-injury comparison where statistically significant difference was found	Rostrocaudal position	p	F(df, error df)
Contusion	Dorsal	3 hr vs. 24 hr	2 mm rostral	0.007	F(2, 24) = 14.278
		3 hr vs. 7d	5 mm rostral	0.033	F(2, 23) = 3.656
			4 mm rostral	0.003	F(2, 24) = 6.995
			3 mm rostral	0.002	F(2, 24) = 7.981
			2 mm rostral	0.00006	F(2, 24) = 14.278
			2 mm caudal	0.013	F(2, 23) = 4.938
			3 mm caudal	0.05	F(2, 23) = 3.458
			4 mm caudal	0.003	F(2, 23) = 7.147
			5 mm caudal	0.032	F(2, 23) = 3.719
	Lateral	3 hr vs. 24 hr	4 mm caudal	0.0002	F(2, 23) = 3.529
			3 mm caudal	0.037	F(2, 23) = 3.529
			2 mm caudal	0.038	F(2, 23) = 3.635
		3hr vs. 7d	4 mm caudal	0.002	F(2, 23) = 3.529
Distraction	Lateral	24 hr vs. 7d	epicentre	0.041	F(2, 27) = 3.414
			1 mm caudal	0.044	F(2, 27) = 3.308

and subacute injury period. Our primary tool in achieving this goal was a binary damage mask that was generated by examining if the longitudinal diffusivity in each location was appreciably lower than an uninjured control value. It is notable that relying on conventional T2-weighted images would not have highlighted white matter damage, since the T2-weighted image contrast was fairly uniform in the white matter of injured cords (see Appendix). However, T2 contrast in areas of damage may be improved in vivo, without the confounding effects of fixation which alters the T2 contrast and shrinks the extracellular space, which can alter the detection of edema in ex vivo tissues. In vivo T2

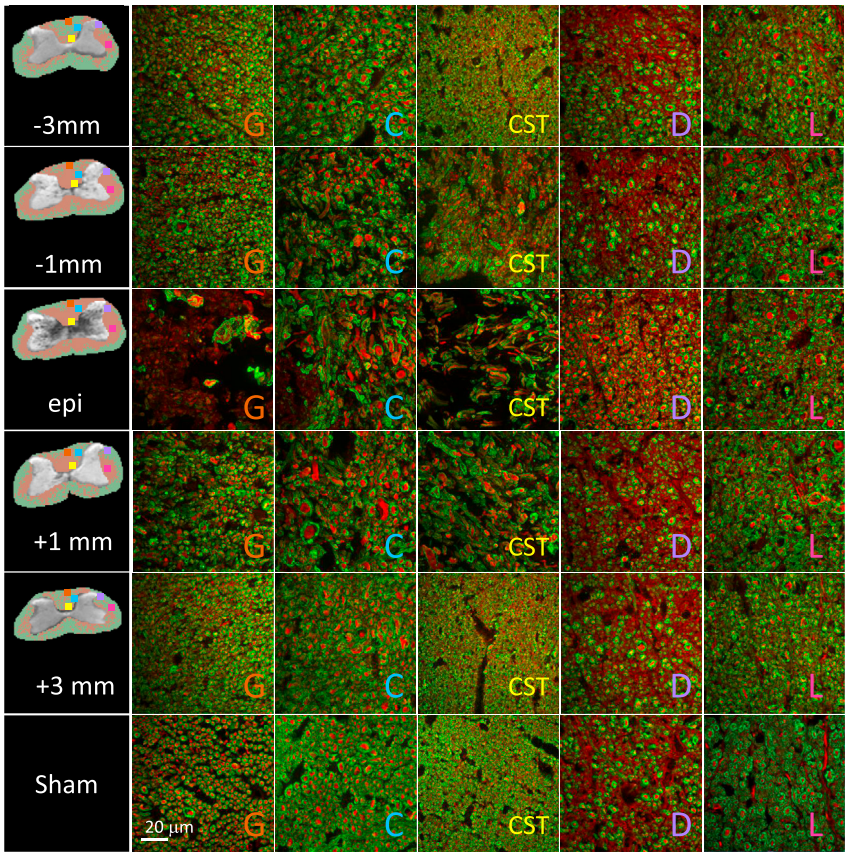

Fig. 8. Histology images of 3 h post-injury contusion cord. Representative histology images on sections immunostained for axon (NF/Tub/SMI312, red) and myelin (MBP, green), for a representative cord in the contusion 3 h post-injury group. Each row corresponds to a different rostrocaudal location (rostral: −3 mm, −1 mm, epicentre, and caudal +1, +3 mm), and each column shows a different location on the axial slice (G: fasciculus gracilis, C: fasciculus cuneatus, CST: corticospinal tract, D: dorsolateral white matter, L: lateral white matter). The left hand column shows the corresponding white matter damage map predicted by D_{long} overlaid on the TrW image (light red: damage, light green: normal appearing), with the approximate locations of the micrographs depicted as squares whose color corresponds to the region label. Micrographs of a sham uninjured cord are depicted for reference on the bottom row.

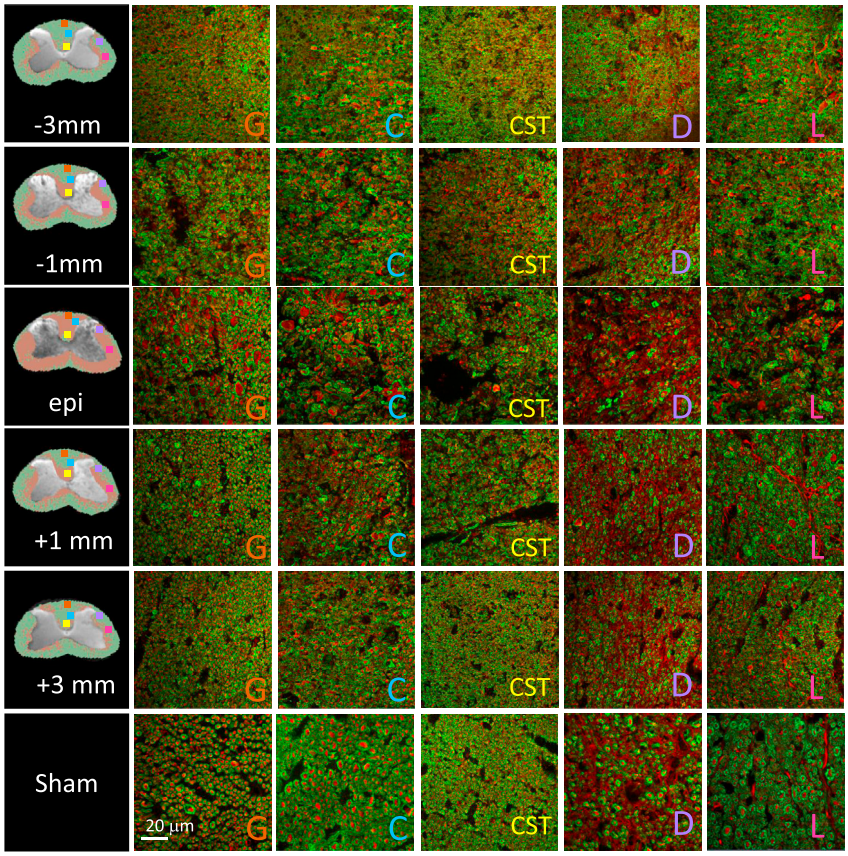

Fig. 9. Histology images of 3 h post-injury dislocation cord. Representative images on sections immunostained for axon (NF/Tub/SMI312, red) and myelin (MBP, green), for a representative cord in the dislocation 3 h post-injury group. Each row corresponds to a different rostrocaudal location (rostral: −3 mm, −1 mm, epicentre, and caudal +1, +3 mm), and each column shows a different location on the axial slice (G: fasciculus gracilis, C: fasciculus cuneatus, CST: corticospinal tract, D: dorsolateral white matter, L: lateral white matter). The left hand column shows the corresponding white matter damage map predicted by D_{long} overlaid on the TrW image (light red: damage, light green: normal appearing), with the approximate locations of the micrographs depicted as squares whose color corresponds to the region label. Micrographs of a sham uninjured cord are depicted for reference on the bottom row.

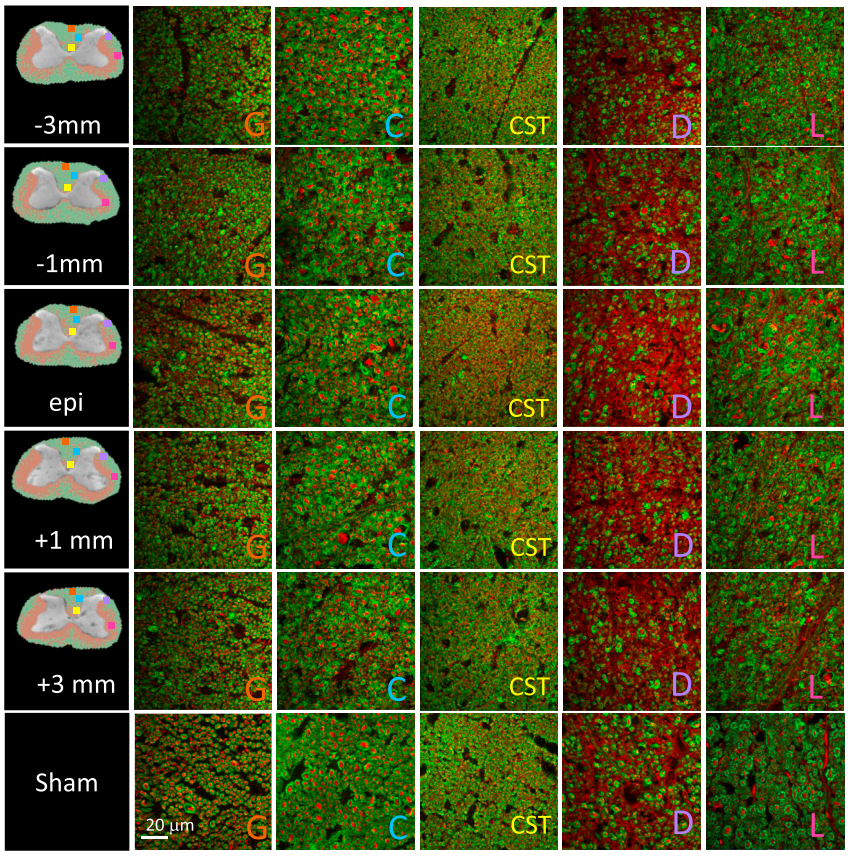

Fig. 10. Histology images of 3 h post-injury distraction cord. Representative images on sections immunostained for axon (NF/Tub/SMI312, red) and myelin (MBP, green), for a representative cord in the distraction 3 h post-injury group. Each row corresponds to a different rostrocaudal location (rostral: −3 mm, −1 mm, epicentre, and caudal +1, +3 mm), and each column shows a different location on the axial slice (G: fasciculus gracilis, C: fasciculus cuneatus, CST: corticospinal tract, D: dorsolateral white matter, L: lateral white matter). The left hand column shows the corresponding white matter damage map predicted by D_{long} overlaid on the TrW image (light red: damage, light green: normal appearing), with the approximate locations of the micrographs depicted as squares whose color corresponds to the region label. Micrographs of a sham uninjured cord are depicted for reference on the bottom row.

abnormalities are a good indicator of the presence of injury, but is not a good predictor of outcome (Dalkilic et al., 2018). Hemorrhage has been related to the severity of functional outcomes in human SCI studies (Dalkilic et al., 2018), but our results suggest that hemorrhage area suffers from higher variability and a smaller rostrocaudal extent which may make it less useful in predicting outcome, as compared to DTI-derived WM damage area. Longitudinal diffusivity was found to be the most effective metric to determine the white matter damage map, which mirrors the robust correlation that other researchers have found between longitudinal diffusivity and microstructural damage to spinal cord white matter (Loy et al., 2007; Kim et al., 2009; Deo et al., 2006; Kozlowski et al., 2008). Fractional anisotropy produced damage maps that were similar in shape but were dimensionally smaller, perhaps due to a lower specificity since it is influenced by both D_{trans} and D_{long}. Transverse diffusivity was the least useful due to a small dynamic range between injured and uninjured values, which may be related to its intrinsically lower SNR. However, D_{trans} has been reported to correlate with myelin changes, and therefore changes in D_{trans} may become more robust past the acute stage of injury where demyelination becomes a major feature in disease progression.

It may be argued that ignoring the specific absolute values of longitudinal diffusivity misses the opportunity to gain more information about the injury severity on a per pixel basis, as it has been shown that the value of D_{long} is negatively correlated with histopathological markers of axonal damage (Budde et al., 2007; Loy et al., 2007; Kim et al., 2009). However, interpreting differences between two anomalous values of longitudinal diffusivity is challenging, since there is no proven stoichiometric relationship between longitudinal diffusivity and an underlying microstructural measure of severity. As one author eloquently states (Jones et al., 2013), "mapping diffusion-weighted MRI data further onto specific microstructural traits is a difficult problem with non-unique solutions, each of which requires strong modeling assumptions." Our goal was simply to promote an analysis tool which would highlight the spatial patterns of injury that could be easily applied in clinical practice, simply by considering any D_{long} that is different from uninjured values to be a general measure of neuronal damage. Injury severity is measured using this approach by examining the size and extent of the damage volume. However, the method may also be extended to distinguish between "less damaged" and "more damaged" areas by setting two threshold values below the normal values to classify the ordinal degree of damage.

The success of generating a white matter damage map relies on the a priori estimate of the uninjured D_{long} value within the region. This is easily done for animal studies through the analysis of a control set of subjects, but for a human patient this is less tractable due to potentially high intersubject variability of DTI values in the uninjured cord. This issue may potentially be solved by using the diffusion metrics taken at a vertebral level that is far away from the injury epicentre as reference. Any approach to defining a threshold value will require careful normalization, as some research (Martin et al., 2017) has found approximately a 17% variation in fractional anisotropy along the normal human cervical cord ($N = 42$), as well as a statistically significant effect of age on fractional anisotropy. The D_{long} cutoff value that was chosen for generating the white matter damage map represents a tradeoff between specificity and sensitivity. Conceivably, there may be a better choice of cutoff value that optimizes this balance, but this is not possible without intensive histology quantification to obtain the necessary estimates of sensitivity.

While histology was acquired in representative cords and related to the corresponding D_{long}-predicted white matter damage maps, further histological analysis would be very beneficial to validate the damage patterns shown by the DTI data, as well as to understand the underlying changes to the white matter microstructure. In particular, a gold-standard measure of the margin between damaged and spared tissue could potentially be derived from histology in order to truly assess the validity of our approach. However, several challenges must be surmounted to complete such a task, not least of which is the large amount of labor in imaging and analyzing the histology sections at a high enough

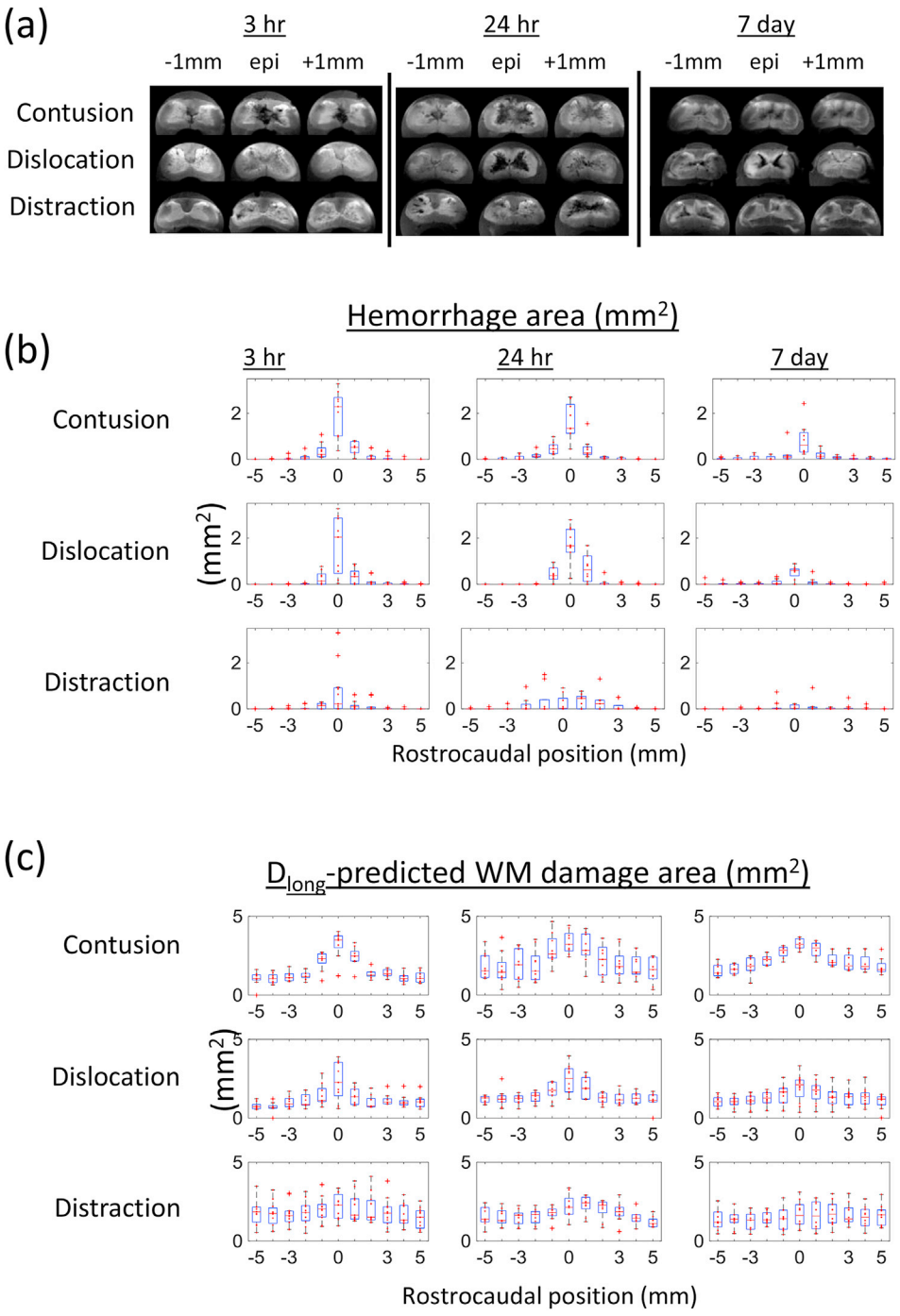

Fig. 11. Hemorrhage and comparison with D_{long}-predicted white matter damage. a) The hypointensities on trace-weighted images were considered to be due to hemorrhage, showing differences across injury mechanism and timepoint b) Boxplots showing hemorrhage areas versus rostrocaudal position. c) Boxplots showing area of D_{long} predicted white matter damage.

magnification to resolve individual axon and myelin sheath structure, while sampling densely and uniformly enough to determine the margin of injury across each tissue section. In particular, standard histological quantification methods such as myelinated axon counting would be infeasible to perform manually, with such a large amount of data required. Aside from these practical hurdles, choosing the appropriate histology metric to characterize damage is a research frontier in itself, since the microstructural hallmarks of white matter damage will change over time and depend on the injury mechanism. For example, damage in the acute stage may be characterized by ovoid swelling of axons ("beading", as described in (Budde and Frank, 2010) without much loss in myelin, whereas secondary injury at chronic time points result in wholesale loss in axons and myelin (Chen et al., 2015). The relatively higher neuronal tissue density found in the dislocation/distraction histology versus the wider spaces in the contusion example may point to a qualitatively different nature of microstructural damage. DTI is potentially sensitive to differences in damage due to time and mechanism, but specificity of the DTI signal remains a challenge. Automation and machine learning approaches to quantifying white matter microstructure may play a role in overcoming these challenges. For example, Zaimi et al. (2018) show the potential for using deep learning approaches to quantify axon parameters such as axonal density, radius, and myelin thickness.

The spatial patterns of white matter damage predicted by DTI in this study both corroborate previous findings, as well as contribute new observations on how the injury mechanisms differ. Contusion produces an initial injury that emanates outward from the central canal in a radial fashion, which corresponds to our finding of greater release of β-APP in the corticospinal tract versus the rest of the dorsal horn at 3 h post-injury (Choo et al., 2008). The centrifugal pattern of damage has also been observed in a variety of other histological and modeling studies (Ma et al., 2001; Blight and Decrescito, 1986), as well as previous DTI studies in the hyperacute phase of contusive injury (Loy et al., 2007). At the outer extents of the studied cord levels, contusion damage extended caudally in the corticospinal tract and rostrally in the gracile fasciculus, aligning with the directionality of axonal degeneration within these tracts. This observation predicts our previous finding that the density of myelinated axon degeneration at 8 weeks post-injury preferentially spread rostrally in the gracilis and caudally in the CST (Chen et al., 2015). Contusion showed the largest volume of damage versus the other injury mechanisms by 7 days post-injury, whereas the damage volume in the distraction and dislocation groups was smaller and experienced some normalization by that time. This is somewhat at odds with our previous histopathological findings of dislocation producing a more pronounced secondary injury at 3 h post-impact (Choo et al., 2008), and a greater degree of functional impairment at 8 weeks post injury (Chen et al., 2015). However, it is possible that pathophysiological changes in contusion models may continue past the first week, as shown in previous literature (see for example (Basso et al., 1996), where locomotor recovery tests show a plateau after approximately 3 weeks in a weight drop contusion model). Dislocation damage maps showed initial insult to the CST, lateral, and ventrolateral white matter, consistent with the high degree of lateral column involvement in 3 h and 8 week histology found previously (Choo et al., 2008; Chen et al., 2015). Von-Mises stress and maximum principal strain in a previous finite-element model also had high involvement of the lateral regions for dislocation injuries (Khuyagbaatar et al., 2016). Interestingly, the damage occurrence ratio maps seem to show that the gracile fasciculus experiences less damage than other dorsal tracts in dislocation injury. The size of the damaged volume for lateral white matter was the largest at 24 h, but shrunk by day 7 across all rostrocaudal positions, with a slight emphasis on the rostral end. This apparent reduced severity of the dislocation injuries at 7 days post-injury may be due to a potential 'survival bias', as four animals reached humane endpoint prior to 7 days post-injury. Animals of equivalent severity in the 3 h and 24 h groups, however, would have been included in those respective analyses. Distraction damage predicted by D_{long} was shown to be less focal and more distributed rostrocaudally, a finding that fits well with previous work (Khuyagbaatar et al., 2016; Chen et al., 2015). In terms of transverse location, distraction damage was most highly associated with lateral and ventrolateral white matter, which was also shown previously with histopathology (Choo et al., 2007).

There are several limitations to this study. Only six diffusion directions were used in the scanning protocol which represents the minimum number to generate DTI metrics, whereas more directions are recommended to increase the robustness of the results. Delineation of the WM/GM boundary was difficult in the low contrast conditions near the injury epicenter, which will introduce more variability in the injured D_{long} area fraction. Ex vivo scans were performed to ensure high SNR and avoid the numerous artifacts that would arise in vivo (motion and susceptibility artifacts, for example). Therefore, serial measurements on the same subject over time was not possible, and we may be missing out on injury processes that would only be apparent in vivo. The ex vivo nature of this work, as well as the potential difficulty of finding normative reference values in actual patients limit this approach's current applicability to clinical translation.

Moreover, it is difficult to rank the injury models by their severity, since it may be impossible to make the applied stress magnitudes equal across injury mechanisms, despite preliminary work to produce injuries of similar functional deficits. This difficulty precluded any statistical analysis between injury models, resulting in a descriptive comparison of the injury models based on qualitative observations of the damage occurrence ratio maps. The ability of longitudinal diffusivity in resolving different input severities through histological or behavioural tests has been successful in previous studies (notably Kim et al. (2012) and Loy et al. (2007), specifically because varying degrees of force were produced with the same injury mechanism. However, the problem with comparing across mechanisms is the impossibility of knowing if the actual energies delivered to the spinal cord are equivalent in each mechanism. Ideally, the total energy applied to the cord during the mechanical insult should be kept constant across mechanism; therefore only the distribution and direction of internal stresses and strains within the cord would be different. Despite our inability to quantitatively compare the injury mechanisms, we contend that focusing on the general shape of injury is the appropriate analysis, since the direction and distribution of forces and stresses during injury are the main differentiators between injury mechanisms, regardless of the inability to control for injury severity.

5. Conclusion

We have demonstrated that DTI can be used to perceive differences between primary injury mechanisms in SCI, through examination of the spatial pattern of cord areas with abnormal DTI metrics. Less emphasis was given to the absolute values of the DTI metrics, to avoid the need of interpreting a certain diffusivity or anisotropy metric as a measure of injury severity, opting instead to assign classifications of "damaged" and "normal" based on DTI measures that were significantly different from normative values. Damage classification was most robust using thresholds in the longitudinal diffusivity, which supports prior studies which have found that D_{long} is the most robust diffusion MRI indicator of damage in spinal cord injury. Our analysis of three different injury models at three different acute time points has yielded a dataset which both corroborates and complements previous histopathological and behavioural studies. The use of subject-specific white matter damage maps and aggregate damage occurrence ratio maps clearly elucidates the overall geometric pattern of damage on the individual and group levels, which is normally obscured by conventional ROI analysis or quantification of isolated histological windows. This work represents a first step in adopting the use of the primary injury mechanism as a clinical prognostic factor in SCI, which may help to inform the trialing of existing neuroprotective treatment candidates, the development of new therapies as well as personalize the management of SCI for the individual patient.

Acknowledgments

This work was supported by the Wings for Life Spinal Cord Research Foundation for financial support in the form of a research grant. Additional financial support from the Blusson Integrated Cures Partnership and CIHR is acknowledged.

Appendix A. Supplementary data

Supplementary data to this article can be found online at https://doi.org/10.1016/j.neuroimage.2018.10.067.

References

Aguet, F., Ville, D.V.D., Unser, M., 2008 Jul. Model-based 2.5-D deconvolution for extended depth of field in brightfield microscopy. IEEE Trans. Image Process. 17 (7), 1144–1153.

Basso, D.M., Beattie, M.S., Bresnahan, J.C., 1996 Jun 1. Graded histological and locomotor outcomes after spinal cord contusion using the NYU weight-drop device versus transection. Exp. Neurol. 139 (2), 244–256.

Bhatnagar, T., Liu, J., Yung, A., Cripton, P.A., Kozlowski, P., Oxland, T., 2016 Apr 1. In vivo measurement of cervical spinal cord deformation during traumatic spinal cord injury in a rodent model. Ann. Biomed. Eng. 44 (4), 1285–1298.

Blight, A.R., Decrescito, V., 1986 Sep 1. Morphometric analysis of experimental spinal cord injury in the cat: the relation of injury intensity to survival of myelinated axons. Neuroscience 19 (1), 321–341.
Budde, M.D., Frank, J.A., 2010 Aug 10. Neurite beading is sufficient to decrease the apparent diffusion coefficient after ischemic stroke. Proc. Natl. Acad. Sci. Unit. States Am. 107 (32), 14472–14477.
Budde, M.D., Kim, J.H., Liang, H.-F., Schmidt, R.E., Russell, J.H., Cross, A.H., et al., 2007. Toward accurate diagnosis of white matter pathology using diffusion tensor imaging. Magn. Reson. Med. 57 (4), 688–695.
By, S., Smith, A.K., Dethrage, L.M., Lyttle, B.D., Landman, B.A., Creasy, J.L., et al., 2016 Dec 1. Quantifying the impact of underlying measurement error on cervical spinal cord diffusion tensor imaging at 3T. J. Magn. Reson. Imag. 44 (6), 1608–1618.
Canny, J.A., 1986 Nov. Computational approach to edge detection. IEEE Trans. Pattern Anal. Mach. Intell. (6), 679–698. PAMI-8.
Chen, K., Liu, J., Assinck, P., Bhatnagar, T., Streijger, F., Zhu, Q., et al., 2015 Dec 16. Differential histopathological and behavioral outcomes eight weeks after rat spinal cord injury by contusion, dislocation, and distraction mechanisms. J. Neurotrauma 33 (18), 1667–1684.
Cheran, S., Shanmuganathan, K., Zhuo, J., Mirvis, S.E., Aarabi, B., Alexander, M.T., et al., 2011 Aug 29. Correlation of MR diffusion tensor imaging parameters with ASIA motor scores in hemorrhagic and nonhemorrhagic acute spinal cord injury. J. Neurotrauma 28 (9), 1881–1892.
Choo, A.M., Liu, J., Lam, C.K., Dvorak, M., Tetzlaff, W., Oxland, T.R., 2007 Mar 1. Contusion, dislocation, and distraction: primary hemorrhage and membrane permeability in distinct mechanisms of spinal cord injury. J. Neurosurg. Spine 6 (3), 255–266.
Choo, A.M., Liu, J., Dvorak, M., Tetzlaff, W., Oxland, T.R., 2008 Aug. Secondary pathology following contusion, dislocation, and distraction spinal cord injuries. Exp. Neurol. 212 (2), 490–506.
Choo, A.M.-T., Liu, J., Liu, Z., Dvorak, M., Tetzlaff, W., Oxland, T.R., 2009 Jun 30. Modeling spinal cord contusion, dislocation, and distraction: characterization of vertebral clamps, injury severities, and node of Ranvier deformations. J. Neurosci. Methods 181 (1), 6–17.
Cohen-Adad, J., Benali, H., Hoge, R.D., Rossignol, S., 2008 Apr 1. In vivo DTI of the healthy and injured cat spinal cord at high spatial and angular resolution. Neuroimage 40 (2), 685–697.
Cohen-Adad, Y., Anaby, D., Morozov, D., 2017 Mar 1. Diffusion MRI of the spinal cord: from structural studies to pathology. NMR Biomed. 30 (3) n/a-n/a.
Cook, R.D., Weisberg, S., 1982. Residuals and Influence in Regression. Chapman and Hall, New York [Internet][cited 2018 Jan 16]. Available from. http://conservancy.umn.edu/handle/11299/37076.
Dalkilic, T., Fallah, N., Noonan, V.K., Salimi Elizei, S., Dong, K., Belanger, L., et al., 2018 Feb 1. Predicting injury severity and neurological recovery after acute cervical spinal cord injury: a comparison of cerebrospinal fluid and magnetic resonance imaging biomarkers. J. Neurotrauma 35 (3), 435–445.
Deo, A.A., Grill, R.J., Hasan, K.M., Narayana, P.A., 2006. In vivo serial diffusion tensor imaging of experimental spinal cord injury. J. Neurosci. Res. 83 (5), 801–810.
Ellingson, B.M., Schmit, B.D., Ulmer, J.L., Kurpad, S.N., 2008. Diffusion tensor magnetic resonance imaging in spinal cord injury. Concepts Magn. Reson. 32A (3), 219–237.
Ellingson, B.M., Schmit, B.D., Kurpad, S.N., 2010 Jul 23. Lesion growth and degeneration patterns measured using diffusion tensor 9.4-T magnetic resonance imaging in rat spinal cord injury. J. Neurosurg. Spine 13 (2), 181–192.
Figley, C.R., Stroman, P.W., 2007. Investigation of human cervical and upper thoracic spinal cord motion: implications for imaging spinal cord structure and function. Magn. Reson. Med. 58 (1), 185–189.
Hendrix, P., Griessenauer, C.J., Cohen-Adad, J., Rajasekaran, S., Cauley, K.A., Shoja, M.M., et al., 2015 Jan 1. Spinal diffusion tensor imaging: a comprehensive review with emphasis on spinal cord anatomy and clinical applications. Clin. Anat. 28 (1), 88–95.
Jasiński, K., Młynarczyk, A., Latta, P., Volotovskyy, V., Węglarz, W.P., Tomanek, B., 2012 Jan. A volume microstrip RF coil for MRI microscopy. Magn. Reson. Imaging 30 (1), 70–77.
Jones, D.K., Knösche, T.R., Turner, R., 2013 Jun. White matter integrity, fiber count, and other fallacies: the do's and don'ts of diffusion MRI. Neuroimage 73, 239–254.
Khuyagbaatar, B., Kim, K., Man Park, W., Hyuk Kim, Y., 2016 Jun 22. Biomechanical behaviors in three types of spinal cord injury mechanisms. J. Biomech. Eng. 138 (8), 081003-081003–7.
Kim, J.H., Loy, D.N., Liang, H.-F., Trinkaus, K., Schmidt, R.E., Song, S.-K., 2007. Noninvasive diffusion tensor imaging of evolving white matter pathology in a mouse model of acute spinal cord injury. Magn. Reson. Med. 58 (2), 253–260.
Kim, J.H., Loy, D.N., Wang, Q., Budde, M.D., Schmidt, R.E., Trinkaus, K., et al., 2009 Dec 14. Diffusion tensor imaging at 3 hours after traumatic spinal cord injury predicts long-term locomotor recovery. J. Neurotrauma 27 (3), 587–598.
Kim, J.H., Song, S.-K., Burke, D.A., Magnuson, D.S.K., 2012 May. Comprehensive locomotor outcomes correlate to hyperacute diffusion tensor measures after spinal cord injury in the adult rat. Exp. Neurol. 235 (1), 188–196.
Koskinen, E., Brander, A., Hakulinen, U., Luoto, T., Helminen, M., Ylinen, A., et al., 2013 Jun 13. Assessing the state of chronic spinal cord injury using diffusion tensor imaging. J. Neurotrauma 30 (18), 1587–1595.
Kozlowski, P., Raj, D., Liu, J., Lam, C., Yung, A.C., Tetzlaff, W., 2008 Jun 1. Characterizing white matter damage in rat spinal cord with quantitative MRI and histology. J. Neurotrauma 25 (6), 653–676.
Loy, D.N., Kim, J.H., Xie, M., Schmidt, R.E., Trinkaus, K., Song, S.-K., 2007 Jun. Diffusion tensor imaging predicts hyperacute spinal cord injury severity. J. Neurotrauma 24 (6), 979–990.
Ma, M., Basso, D.M., Walters, P., Stokes, B.T., Jakeman, L.B., 2001 Jun 1. Behavioral and histological outcomes following graded spinal cord contusion injury in the C57bl/6 mouse. Exp. Neurol. 169 (2), 239–254.
Martin, A.R., Leener, B.D., Cohen-Adad, J., Cadotte, D.W., Kalsi-Ryan, S., Lange, S.F., et al., 2017 Jun 1. Clinically feasible microstructural MRI to quantify cervical spinal cord tissue injury using DTI, MT, and t2*-weighted imaging: assessment of normative data and reliability. Am. J. Neuroradiol. 38 (6), 1257–1265.
Myronenko, A., Song, X., 2010 Dec. Point set registration: coherent point Drift. IEEE Trans. Pattern Anal. Mach. Intell. 32 (12), 2262–2275.
Nossin-Manor, R., Duvdevani, R., Cohen, Y., 2007 Mar 1. Spatial and temporal damage evolution after hemi-crush injury in rat spinal cord obtained by high b-value q-space diffusion magnetic resonance imaging. J. Neurotrauma 24 (3), 481–491.
Pickett, G.E., Campos-benitez, M., Keller, J.L., Duggal, N., 2006 Apr 1. Epidemiology of traumatic spinal cord injury in Canada. Spine 31 (7), 799–805.
Russell, C.M., Choo, A.M., Tetzlaff, W., Chung, T.-E., Oxland, T.R., 2012 May 20. Maximum principal strain correlates with spinal cord tissue damage in contusion and dislocation injuries in the rat cervical spine. J. Neurotrauma 29 (8), 1574–1585.
Sasiadek, M.J., Szewczyk, P., Bladowska, J., 2012 Jun 1. Application of diffusion tensor imaging (DTI) in pathological changes of the spinal cord. Med. Sci. Monit. Int. Med. J. Exp. Clin. Res. 18 (6), RA73–R79.
Schindelin, J., Arganda-Carreras, I., Frise, E., Kaynig, V., Longair, M., Pietzsch, T., et al., 2012 Jun 28. Fiji: an open-source platform for biological-image analysis. Nat. Methods 9 (7), 676–682.
Sekhon, L.H., Fehlings, M.G., 2001 Dec 15. Epidemiology, demographics, and pathophysiology of acute spinal cord injury. Spine 26 (24 Suppl), S2–S12.
Shanmuganathan, K., Zhuo, J., Chen, H.H., Aarabi, B., Adams, J., Miller, C., et al., 2017 Apr 6. Diffusion tensor imaging parameter obtained during acute blunt cervical spinal cord injury in predicting long-term outcome. J. Neurotrauma 34 (21), 2964–2971.
Smith, S.A., Pekar, J.J., van Zijl, P.C.M., 2012. Advanced MRI strategies for assessing spinal cord injury. Handb. Clin. Neurol. 109, 85–101.
Stroman, P.W., Wheeler-Kingshott, C., Bacon, M., Schwab, J.M., Bosma, R., Brooks, J., et al., 2014 Jan 1. The current state-of-the-art of spinal cord imaging: Methods. Neuroimage 84, 1070–1081.
Tator, C.H., 2006 Nov 1. Review of treatment trials in human spinal cord injury: issues, difficulties, and recommendations. Neurosurgery 59 (5), 957–987.
Tu, T.-W., Kim, J.H., Yin, F.Q., Jakeman, L.B., Song, S.-K., 2013. The impact of myelination on axon sparing and locomotor function recovery in spinal cord injury assessed using diffusion tensor imaging. NMR Biomed. 26 (11), 1484–1495.
Xu, J., Li, H., Harkins, K.D., Jiang, X., Xie, J., Kang, H., et al., 2014 Dec 1. Mapping mean axon diameter and axonal volume fraction by MRI using temporal diffusion spectroscopy. Neuroimage 103, 10–19.
Zaimi, A., Wabartha, M., Herman, V., Antonsanti, P.-L., Perone, C.S., Cohen-Adad, J., 2018 Feb 28. AxonDeepSeg: automatic axon and myelin segmentation from microscopy data using convolutional neural networks. Sci. Rep. 8 (1), 3816.